Monthly Notices
of the
ROYAL ASTRONOMICAL SOCIETY

Mon. Not. R. Astron. Soc. **420,** 2162–2169 (2012) doi:10.1111/j.1365-2966.2011.20182.x

Multiresolution internal template cleaning: an application to the *Wilkinson Microwave Anisotropy Probe* 7-yr polarization data

R. Fernández-Cobos,[1,2⋆] P. Vielva,[1] R. B. Barreiro[1] and E. Martínez-González[1]

[1]*Instituto de Física de Cantabria, CSIC-Universidad de Cantabria, Avda. de los Castros s/n, 39005 Santander, Spain*
[2]*Dpto de Física Moderna, Universidad de Cantabria, Avda. los Castros s/n, 39005 Santander, Spain*

Accepted 2011 November 10. Received 2011 November 7; in original form 2011 June 9

ABSTRACT

The cosmic microwave background (CMB) radiation data obtained by different experiments contain, besides the desired signal, a superposition of microwave sky contributions. Using a wavelet decomposition on the sphere, we present a fast and robust method to recover the CMB signal from microwave maps. We present an application to the *Wilkinson Microwave Anisotropy Probe* (*WMAP*) polarization data, which shows its good performance, particularly in very polluted regions of the sky. The applied wavelet has the advantages that it requires little computational time in its calculations, it is adapted to the HEALPIX pixelization scheme and it offers the possibility of multiresolution analysis. The decomposition is implemented as part of a fully internal template fitting method, minimizing the variance of the resulting map at each scale. Using a χ^2 characterization of the noise, we find that the residuals of the cleaned maps are compatible with those expected from the instrumental noise. The maps are also comparable to those obtained from the *WMAP* team, but in our case we do not make use of external data sets. In addition, at low resolution, our cleaned maps present a lower level of noise. The E-mode power spectrum $C_\ell^{\rm EE}$ is computed at high and low resolutions, and a cross-power spectrum $C_\ell^{\rm TE}$ is also calculated from the foreground reduced maps of temperature given by *WMAP* and our cleaned maps of polarization at high resolution. These spectra are consistent with the power spectra supplied by the *WMAP* team. We detect the E-mode acoustic peak at $\ell \sim 400$, as predicted by the standard ΛCDM model. The B-mode power spectrum $C_\ell^{\rm BB}$ is compatible with zero.

Key words: methods: data analysis – cosmic background radiation.

1 INTRODUCTION

Component separation is critical in the analysis of cosmic microwave background (CMB) data. A good characterization of the data is a prerequisite to the adequate estimation of cosmological parameters. This becomes crucial when, as happens in B-mode detection experiments, foreground amplitudes are well above the signal (e.g. Tucci et al. 2005). Two physical galactic processes are major contaminants to the CMB polarized signal: synchrotron radiation and thermal dust. Both appear at large scales, both are highly anisotropic and the spatial variation of their emissivity is smooth. Moreover, extragalactic emission also contaminates this cosmological signal; point sources and clusters are compact objects, roughly isotropically distributed in the sky, and every single object has a particular frequency dependence. Most methods of component separation take into account only diffuse components, assuming that we have previously masked the brightest point sources or subtracted them by, typically, fitting approaches (see Herranz & Vielva 2010, for a recent review).

Current and future experiments (Kogut et al. 2006; Charlassier et al. 2008; Grainger et al. 2008; Rubiño-Martín et al. 2010; Brown et al. 2009; Sievers et al. 2009; Arnold et al. 2010) are able to measure CMB polarization anisotropies with such precision that foreground contamination has become the major limitation when we try to analyse the data. This is the principal reason for investing effort and time in developing new techniques for separating components. The goal of all the proposed methods is to separate or, at least, to identify CMB anisotropies from the other components. The range of proposals includes internal linear combinations (ILCs), Bayesian methods and independent component analysis (see Delabrouille & Cardoso 2007, for a recent review).

There is an abundant body of literature that includes applications of the various methods related to some current polarization experiments, such as, for example, *Planck* (Baccigalupi et al. 2004; Leach et al. 2008; Betoule et al. 2009; Efstathiou, Gratton & Paci 2009) and the *Wilkinson Microwave Anisotropy Probe* (*WMAP*; Eriksen et al.

⋆E-mail: cobos@ifca.unican.es

2006, 2008; Bonaldi et al. 2007; Maino et al. 2007; Delabrouille et al. 2009; Kim, Naselsky & Christensen 2009; Gold et al. 2011).

The method that we present in this paper can be seen in the context of ILCs, and it is a way of template cleaning in which coefficients are fitted in to the space of a particular wavelet that enables a multiresolution analysis. A fitting by scales allows, in practice, some effective variation of the coefficients in the sky, which is an advantage over template cleaning in real space. In this sense, our approach based on wavelet space effectively lies in between standard linear combination techniques applied in the real space and more sophisticated parametric methods (e.g. Eriksen et al. 2006, 2008; Stivoli et al. 2010).

Our approach is a fast procedure, which especially shows its effectiveness in polluted regions, such as those that appear in polarization experiments.

This paper is structured as follows. The methodology is described in detail in Section 2. We set out an analysis of the low-resolution polarization *WMAP* data in Section 3. In Section 4, we show the treatment for high-resolution *WMAP* data in order to obtain the $C_\ell^{\rm EE}$ and $C_\ell^{\rm TE}$ spectra. Finally, we present the conclusions and discussion in Section 5.

2 METHODOLOGY

In this work, we present a multiresolution internal template cleaning (MITC) method for foreground removal. This is the initial step of the map cleaning process in the SEVEM method of polarization (Martínez-González et al. 2003; Leach et al. 2008).

For many purposes, it is important to have CMB maps at several frequencies instead of a single map. For instance, this would help as a consistency check to verify whether any detected feature of the data is actually monochromatic or not (e.g. the case for non-Gaussianity analysis).

Another advantage of the method is that we do not need a thorough knowledge of foregrounds, because we obtain all the information to construct different templates from the data. Furthermore, this procedure preserves the original resolution of the CMB component. However, the disadvantage is that the internal templates are noisy, so we increase the total noise level when we remove these from the data. For example, this results in an increase in the error bars of the power spectrum at high multipoles. An alternative would be to incorporate external templates, created from data from other independent observations or based on theoretical arguments. However, the current knowledge of foreground emissions, in polarization, is not substantiated with a suitable ancillary data set. For this reason, this option is not considered in this case. This situation might change in the future with information expected to be provided by experiments such as *Planck* (Tauber et al. 2010), the C-Band All-Sky Survey (C-BASS; King et al. 2011) or the Q-U-I Joint Tenerife (QUIJOTE; Rubiño-Martín et al. 2010).

2.1 The HEALPix wavelet

Wavelets are a powerful tool in signal analysis and are extensively used in many astrophysical applications. Several examples of the implementation of component separation methods, which employ very diverse wavelets, can be found in the literature (e.g. Vielva et al. 2003; González-Nuevo et al. 2006; Hansen et al. 2006; Delabrouille et al. 2009; Ghosh et al. 2011). These are localized wavefunctions that allow for a multiresolution treatment of the data. This fact represents an advantage over other component separation methods because it allows us to vary the effective emissivity of foregrounds.

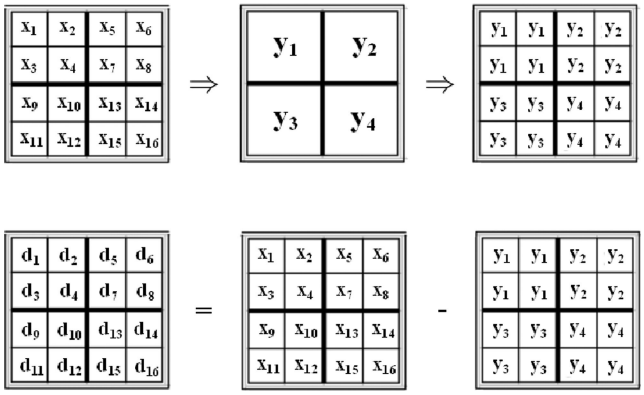

Figure 1. Outline of the construction of the detail coefficients at resolution j (d_i) as a substraction of the approximation coefficients at resolution $j-1$ (y_i), from the approximation coefficients at resolution j (x_i).

We use the so-called HEALPIX wavelet (HW; Casaponsa et al. 2011), a discrete and orthogonal wavelet that provides a multiscale decomposition on the sphere adapted to the HEALPIX pixelization (Górski et al. 2005). The resolution of a map in the HEALPIX tessellation is given in terms of the $N_{\rm side}$ parameter, defined so that the number of pixels needed to cover the sphere is $N = 12N_{\rm side}^2$. The resolution j of a map is a number such that $2^j = N_{\rm side}$. A CMB map is decomposed in the wavelet coefficient space in a series of maps from the resolution of the original map to the lowest resolution considered. All of these maps, except for the lowest resolution map, are called details. The last map is called the approximation, and this is constructed by degrading the original map to the appropriate resolution (i.e. in order to calculate the approximation coefficient at resolution j-1 at a given position i, we take the average of the four daughter pixels at resolution j). Fig. 1 illustrates the way that different detail maps are built. At each resolution j, detail coefficients are calculated as the substraction of the approximation coefficients at resolution j-1 from the approximation coefficients at resolution j. Both this process and the mathematical formalism of this wavelet are carefully explained in Casaponsa et al. (2011), where the HW is used to put constraints on the $f_{\rm NL}$ parameter from the *WMAP* data.

Casaponsa et al. (2011) state that the reconstruction of a map $M(x_i)$ can be written as

$$M(x_i) = \sum_{p=0}^{n_{j_0}-1} \lambda_{j_0,p}\phi_{j_0,p}(x_i) + \sum_{m=1}^{4}\sum_{j=j_0}^{J-1}\sum_{p=0}^{n_j-1} \gamma_{m,j,p}\psi_{m,j,p}(x_i). \quad (1)$$

Here, $\lambda_{j_0,\ell}$ and $\gamma_{m,j,\ell}$ are the approximation and detail coefficients respectively, $\phi_{j,p}(x_i)$ is the scaling function and $\psi_{m,j,p}(x_i)$ refers to the wavelet functions. The j index takes values from the highest resolution J to the approximation resolution j_0.

The advantage of this wavelet with respect to others, in addition to its straightforward implementation, lies in the speed of the involved operations. The computational time for the wavelet decomposition is of the order of the number of pixels ($\sim N_{\rm pix}$) whereas, for example, for the continuous wavelet transform of the spherical Mexican hat wavelet (Martínez-González et al. 2002) or the needlets (Baldi et al. 2009) this time is of the order of $\sim N_{\rm pix}^{3/2}$.

2.2 Template fitting

The signal $\widehat{T}_j(p)$ at resolution j is constructed by subtracting a linear combination of different templates t_{ij} from the original signal T_j, as

follows

$$\widehat{T}_j(p) = T_j(p) - \sum_{i=1}^{N_t} \beta_{ij} t_{ij}(p), \tag{2}$$

where N_t is the total number of templates and p is a pixel index.

An internal template is formed as the difference of two maps of the same resolution, corresponding to different frequencies, in units of thermodynamic temperature.

The variance of the cleaned map is optimally minimized at each scale to obtain the coefficients β_{ij} or, equivalently, the quadratic quantity

$$\chi_j^2 = \sum_p \left\{ \widehat{T}_j(p) C^{-1} [\widehat{T}_j(p)]^t \right\}. \tag{3}$$

Here, C^{-1} is the inverse of the covariance matrix, calculated as the sum of contributions of the CMB and instrumental noise (both from the map to be cleaned and the templates).

From the above discussion, it is obvious that the approach to produce an optimal recovery of the CMB would require a certain knowledge of this signal, via its correlations. However, a more robust estimator, without a priori knowledge of the signal to be estimated, can be built by considering only the instrumental noise correlations.

However, we have checked that the gain in the CMB recovery, by including the information related to the instrumental characteristics is, in practice, very small. Moreover, in some situations (as is the case of the *WMAP* full resolution data; see Section 4), the instrumental-noise information is limited to the autocorrelation. Therefore, we have decided to perform the internal template fitting with uniform weights for all the pixels at each scale, which implies that we minimize the following quantity:

$$E_j = \sum_p \left[T_j(p) - \sum_{i=1}^{N_t} \beta_{ij} t_{ij}(p) \right]^2. \tag{4}$$

Finally, we recover a single map to perform the wavelet synthesis, which can be written as

$$\widehat{T}(\boldsymbol{x}) = T(\boldsymbol{x}) - \sum_{i=1}^{N_t} \sum_{j=1}^{N_{\rm res}} \gamma_{ij}(\boldsymbol{x}) t_{ij}(\boldsymbol{x}). \tag{5}$$

Here, $N_{\rm res}$ denotes the number of involved resolutions and γ_{ij} are some new coefficients, given as linear combinations of β_{ij} coefficients, which are the result of the synthesis process.

3 ANALYSIS OF LOW-RESOLUTION *WMAP* DATA

The instrumental noise in *WMAP* polarization is known to be correlated (Jarosik et al. 2011). Although the *WMAP* data are typically given at a HEALPIX resolution of $N_{\rm side} = 512$, a more accurate version of the pixel-to-pixel correlation is only available at low resolution (i.e. $N_{\rm side} = 16$). Taking into account this difference, we have performed the cleaning of the *WMAP* data in two cases: for low-resolution and high-resolution maps. In this section, we analyse the maps at $N_{\rm side} = 16$.

The *WMAP* data are composed by, at least, a superposition of CMB, synchrotron and thermal dust emissions. The *WMAP* team have proposed a template fitting in the pixel space to clean the foreground emission in the $K_{\rm a}$, Q, V and W maps, using as templates the K band (for the synchrotron) and a low-resolution version of the Finkbeiner, Davis & Schlegel (1999) model for the thermal dust, with polarization direction derived from starlight measurements (Gold et al. 2011).

Table 1. Template cleaning coefficients for Q and U Stokes parameters and DAs for the low-resolution analysis.

Frequency band		$Q1$	$Q2$	$V1$	$V2$
Detail ($j = 4$)	Q Stokes	0.092	0.103	0.036	0.023
	U Stokes	0.074	0.117	0.020	0.048
Approximation ($j = 3$)	Q Stokes	0.244	0.259	0.081	0.125
	U Stokes	0.241	0.236	0.085	0.112

In our approach, we use only a synchrotron template, constructed as K–$K_{\rm a}$. The reason for neglecting the thermal dust template is because a previous analysis in real space shows that its coefficients are much smaller than the corresponding coefficients for the synchrotron template. We clean the Q and U polarization components independently, minimizing the variance of the cleaned maps of the $Q1$, $Q2$, $V1$ and $V2$ differencing assemblies (DAs). The wavelet decomposition is carried out down to resolution $j = 3$ for the data map. Thus, in addition to the approximation, we have a single detail map at $j = 4$. Best-fitting coefficients for the considered DAs are given in Table 1. We apply the *WMAP* polarization analysis mask that excludes 26 per cent of the sky.

3.1 Cleaned maps

Because the CMB polarization signal is clearly subdominant in the *WMAP* low-resolution data, it is hard to establish a criterion to evaluate the goodness of the cleaning process, and to perform comparisons with different solutions.

We have decided to evaluate this goodness by comparing the cleaned map with the expected signal for a noisy sky, following the *WMAP* instrumental noise characteristics. In this sense, a good compatibility with the noise properties would indicate that foregrounds have been satisfactorily reduced.

We generate a set of 10^4 simulations of the noise maps resulting from our MITC method at the Q, V and W frequency bands, $M_r(p)$, with $r \in \{1, \ldots, 10^4\}$, in order to construct a χ^2 distribution. We calculate each value as

$$\chi_r^2 = \sum_{p,q} M_r(p) N_{\rm Obs}^{-1}(p,q) M_r^t(q), \tag{6}$$

where $N_{\rm Obs}$ is the noise correlation matrix. We need the number of simulations to be of the order of a million in order to estimate this matrix so that the distribution converges to the theoretical curve of a χ^2 distribution with as many degrees of freedom as pixels outside the mask in the Q and U maps (in this case, we have 4518 degrees of freedom). This distribution characterizes the expected noise level at each frequency map. We can associate the χ^2 value of the data with relative levels of the signal. We can say that the cleaned maps contain more than just noise (typically foreground residuals, because the CMB is subdominant compared to the noise at these scales) if the data value is much higher than typical values of the distribution. In contrast, we can ensure that our maps are compatible with the expected noise and that residuals are small if the data value falls within the distribution. The χ^2 values for each band and for each DA are listed in Tables 2 and 3, respectively.

Our test is based on the assumption that the CMB contribution is negligible. We have tested that the CMB provides a very small contribution (a shift of $\sim$10 units of χ^2) by generating 10^4 simulations with CMB and instrumental noise of the cleaned maps. These simulations have been used to compute another χ^2 distribution with the

Table 2. Different values of χ^2 computed with our 7-yr cleaned maps per frequency band ($\chi^2_{\rm cleaned}$) and with *WMAP* 7-yr foreground reduced maps per frequency band ($\chi^2_{\rm forered}$).

Frequency band	Q	V	W
$\chi^2_{\rm cleaned}$	4566	4453	4762
$\chi^2_{\rm forered}$	4709	4586	4787

matrix that we have already calculated with only the noise component. When distributions are compared with each other, we observe this typical deviation. Thus, the CMB contribution to the value of the χ^2 of the data is negligible. Therefore, any significant deviation from the mean value has to be assigned to foreground residuals.

An indirect comparison can be made between the *WMAP* procedure and our MITC method through the relative positions of the χ^2 value of the data with respect to the distribution. As seen in Fig. 2, we find that the value of the cleaned maps is fully compatible with instrumental noise at the Q and V frequency bands. At the W band, the χ^2 value of the cleaned data is in the tail of the distribution, probably because of the presence of foreground residuals. The deviation is even larger when the *WMAP* procedure is used. A significant improvement is also found at the Q band because the χ^2 value is shifted from 2σ to 0.5σ when our MITC method is used.

In addition, although we use a template that is noisier than those used by the *WMAP* team, the noise levels of our cleaned maps are lower. We have measured a difference of about 10 per cent in terms of the standard deviation of the data maps (this difference is confirmed by instrumental-noise simulations).

Table 3. Different values of χ^2 computed with our 7-yr cleaned maps per DA.

DA	$Q1$	$Q2$	$V1$	$V2$
$\chi^2_{\rm cleaned}$	4489	4546	4405	4486

In order to check further the apparent excess of signal at the W band obtained by the two approaches, we computed analytically the noise covariance matrix of different combinations of the raw W-band DA maps, which contain, in principle, only a combination of instrumental noise. With these covariance matrices, based on the full-sky covariance matrices of each DA, a χ^2 value of the data maps is obtained. Fig. 3 shows that these maps are still compatible with the expected noise. However, it is significant that all values are to the left of the distribution and that the most deviated values involve $W2$, followed by $W4$. We have also analysed the distribution of the χ^2 values of the single-year foreground reduced maps supplied by the *WMAP* team for each DA at the W band. We have obtained values that deviate more towards the tails for the $W2$ and $W4$ DAs. This could suggest that the characterization of the instrumental noise for these DAs is not good enough.

3.2 Polarization power spectra, $C_\ell^{\rm EE}$ and $C_\ell^{\rm BB}$

We carry out an estimation of the polarization spectrum using our cleaned maps of the $Q1$, $Q2$, $V1$ and $V2$ DAs. A pseudo cross-power spectrum $\hat{D}_\ell^{\rm AB}$, between any two differencing assemblies A and B, can be calculated as

$$\hat{D}_\ell^{\rm AB} = \sum_{\ell'} M_{\ell\ell'}^{\rm AB} |p_{\ell'}|^2 B_{\ell'}^{\rm A} B_{\ell'}^{\rm B} \langle C_{\ell'}^{\rm AB} \rangle + \langle N_\ell^{\rm AB} \rangle, \quad (7)$$

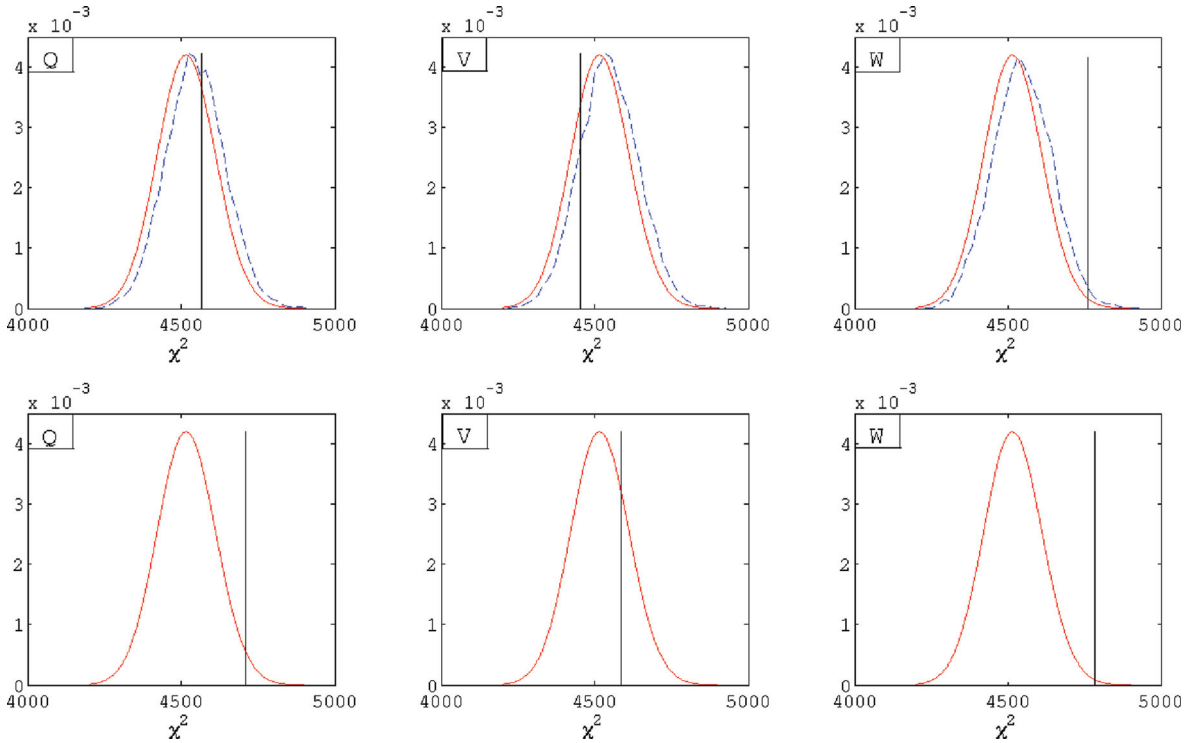

Figure 2. The upper panels show the χ^2 distributions of our cleaned maps and the lower panels present the same results for the *WMAP* procedure. The solid red line corresponds to the theoretical curve of χ^2 with as many degrees of freedom as pixels outside the mask (i.e. the effective number of pixels in the Q and U maps is 4518). The dashed line is the distribution calculated from the simulations of our cleaned maps. The vertical line shows the χ^2 value of the data maps in each case. The columns correspond to different frequency bands: from left to right, Q, V and W bands.

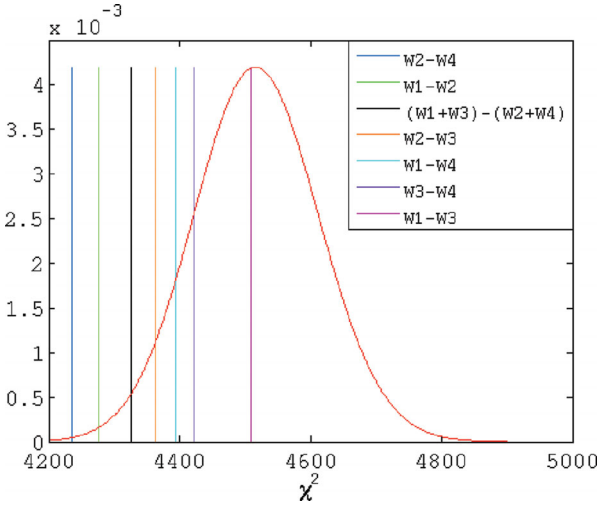

Figure 3. The combinations of the raw W-band maps. The theoretical curve of the χ^2 distribution is represented by a solid red line and the χ^2 values are shown by successive vertical lines: from left to right, $W2$–$W4$, $W1$–$W2$, $(W1+W3)$–$(W2+W4)$, $W2$–$W3$, $W1$–$W4$, $W3$–$W4$ and $W1$–$W3$.

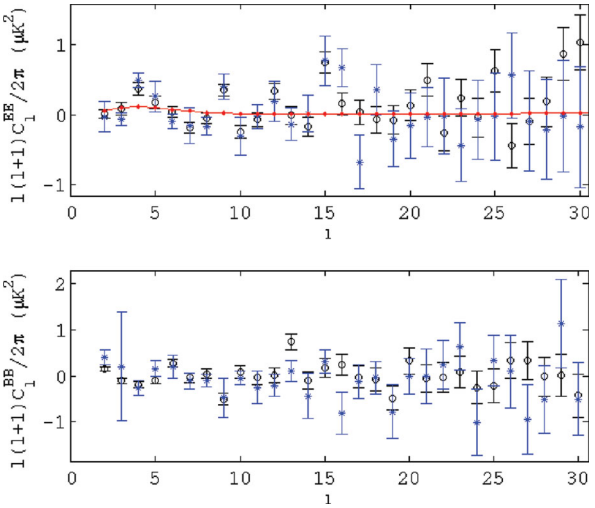

Figure 4. Polarization power spectrum EE (upper panel) and BB (lower panel) for the low-resolution analysis. The circles denote the spectrum supplied by the *WMAP* team and the asterisks represent our estimation. The fiducial model is plotted by the solid line.

where A, B $\in \{Q1, Q2, V1, V2 \mid \mathrm{A} \neq \mathrm{B}\}$. In the case of an EE power spectra,

$$\hat{C}_\ell^{\mathrm{AB}} = \frac{1}{2\ell+1} \sum_{m=-\ell}^{\ell} e_{\ell m}^{\mathrm{A}} e_{\ell m}^{\mathrm{B}*}, \tag{8}$$

where $e_{\ell m}$ are the spherical harmonic coefficients of the E-mode. Assuming a circular beam response, we denote the beam of the A map as B_ℓ^{A} and the window function of the HEALPIX pixel as p_ℓ. In equation (7), $\langle N_\ell^{\mathrm{AB}} \rangle$ is the noise cross-power spectrum. The bias introduced by this term comes from the internal template fitting procedure. It is small and is controlled by simulations. Finally, the

Table 4. Template cleaning coefficients for Q and U Stokes parameters and different frequency bands for the high-resolution analysis.

DA	Template	Stokes	$Q1$	$Q2$	$V2$	$W1$	$W2$	$W4$
Detail ($j=9$)	(K–K_a)	Q Stokes	−0.0175	−0.0067	0.0024	0.0754	0.0072	−0.0222
		U Stokes	0.0525	0.0173	0.0085	−0.0869	0.1171	−0.0562
	($V1$–$W3$)	Q Stokes	−0.0008	0.0023	−0.0015	0.0013	−0.0015	0.0054
		U Stokes	0.0007	0.0006	0.0022	0.0005	−0.0226	−0.0106
Detail ($j=8$)	(K–K_a)	Q Stokes	−0.0238	0.0185	0.0135	−0.0046	0.0076	0.0311
		U Stokes	−0.0080	−0.0176	−0.0059	−0.0513	0.0138	−0.0196
	($V1$–$W3$)	Q Stokes	−0.0044	−0.0003	−0.0008	−0.0048	0.0020	0.0071
		U Stokes	0.0012	0.0028	0.0042	0.0013	0.0030	0.0012
Detail ($j=7$)	(K–K_a)	Q Stokes	0.0006	0.0045	−0.0091	−0.0227	0.0288	−0.0224
		U Stokes	−0.0208	0.0196	0.0038	−0.0263	0.0047	−0.0142
	($V1$–$W3$)	Q Stokes	0.0054	0.0004	−0.0002	−0.0053	−0.0002	0.0069
		U Stokes	−0.0017	0.0006	0.0032	0.0019	−0.0036	0.0009
Detail ($j=6$)	(K–K_a)	Q Stokes	0.0224	−0.0112	−0.0073	0.0302	−0.0057	0.0407
		U Stokes	0.0278	0.0172	0.0104	0.0144	0.01797	0.0076
	($V1$–$W3$)	Q Stokes	0.0079	0.0014	−0.0039	−0.0070	−0.0095	−0.0038
		U Stokes	0.0066	−0.0051	0.0016	−0.0012	−0.0096	0.0179
Detail ($j=5$)	(K–K_a)	Q Stokes	0.0351	0.0729	0.0702	−0.0325	0.0253	−0.1171
		U Stokes	0.0567	0.0523	0.0670	0.1166	0.0255	−0.0225
	($V1$–$W3$)	Q Stokes	−0.0131	0.0012	0.0207	−0.0070	−0.0578	0.0508
		U Stokes	−0.0080	0.0009	−0.0071	−0.0362	−0.0006	0.0363
Detail ($j=4$)	(K–K_a)	Q Stokes	0.2292	0.0571	0.0548	−0.0835	0.3029	−0.2239
		U Stokes	0.0741	0.1172	−0.0844	0.1445	−0.2241	−0.2723
	($V1$–$W3$)	Q Stokes	−0.0708	0.0774	−0.1389	0.0386	0.1316	−0.0135
		U Stokes	−0.0440	0.0359	−0.0397	0.1985	−0.2028	0.2320
Approximation ($j=3$)	(K–K_a)	Q Stokes	0.1732	0.2976	0.1988	0.1413	0.1234	0.2612
		U Stokes	0.1397	0.2315	0.1674	0.1607	0.4529	0.5386
	($V1$–$W3$)	Q Stokes	−0.2852	0.2030	0.6050	0.5513	0.2601	−1.1963
		U Stokes	0.2087	0.1022	−0.0048	0.5052	0.0160	−0.3867

coupling kernel matrix $M_{\ell\ell'}$ is described in Hivon et al. (2002) and, for the case of the polarization components, in appendix A of Kogut et al. (2003). This procedure is usually referred to as the MASTER estimation. An estimator $\hat{C}_\ell$ can be computed as a linear combination of the six different spectra weighted by the inverse of their variances in the following way:

$$\hat{C}_\ell = \left(\sum_i \frac{1}{\sigma_i^2} \right)^{-1} \sum_i \frac{1}{\sigma_i^2} \hat{C}_\ell^i. \quad (9)$$

Here, $i = \mathrm{AB}$ and $\sigma_i^2 = \sigma_\mathrm{A}\sigma_\mathrm{B}$. These variances are given by the *WMAP* team on the Legacy Archive for Microwave Background Data Analysis (LAMBDA) web site.[1]

The resulting power spectra are shown in Fig. 4. From the C_ℓ^{EE} spectrum, we find that most of the values are compatible with zero, so there is almost no signal except perhaps for low multipoles $\ell \lesssim 6$. As expected, the B-mode spectrum C_ℓ^{BB} signal is compatible with zero. Both spectra are compatible with those that the *WMAP* team supplies. Our error bars are larger than those obtained by the *WMAP* team, because we use an estimator that is not optimal, a pseudo-spectrum, whereas the *WMAP* team uses a pixel-base likelihood.

4 ANALYSIS OF HIGH-RESOLUTION *WMAP* DATA

In this section, we analyse *WMAP* data maps at $N_{\mathrm{side}} = 512$. This approach allows us to study the cleaning at smaller scales where, a priori, the correlation of the noise is less important. So, we only take into account the noise covariance matrix of each pixel. In this case, the cleaning method based on the wavelet space is applied using two different internal templates. The first is constructed as K–K_a and accounts for the synchrotron radiation. The second is built as $V1$–$W3$ and attempts to characterize the thermal dust. The V and W DAs to be cleaned have been selected because they have lower noise. As in the low-resolution case, the wavelet decomposition is carried out until resolution $j = 3$ for the approximation map, and hence we have, additionally, six different detail maps in this high-resolution case. Again, the *WMAP* polarization mask is used. Best-fitting coefficients are shown in Table 4.

Using the cleaned Q and U maps, we study the power spectra, C_ℓ^{EE} and C_ℓ^{BB}, as in Section 3. The spectrum error bars are estimated from 10^3 noise simulations. In general, the CMB contribution is negligible compared to the noise contribution. Bins are taken as a weighted average of the multipoles involved. These weights are calculated as the inverse of the variance of each C_ℓ.

The spectra are compatible with those that the *WMAP* team has obtained. Our error bars are larger at high multipoles because, at this scale range, the number of effective cross-spectra is much smaller than the number used by the *WMAP* team (where all the W-band DAs are available). Nevertheless, as seen in Fig. 2, our cleaned maps seem to present a lower level of contamination than those supplied by the *WMAP* team. We expected a better foreground removal because the templates used are closer to the foreground signal distribution across the sky in our case. However, it is not clear whether this could have an impact on the determination of the cosmological parameters. To determine this, we would need to carry out an exhaustive analysis, which is outside the scope of this paper.

Finally, the two points accounting for the largest scales of the spectra are taken from Fig. 4, because the correlation of the noise

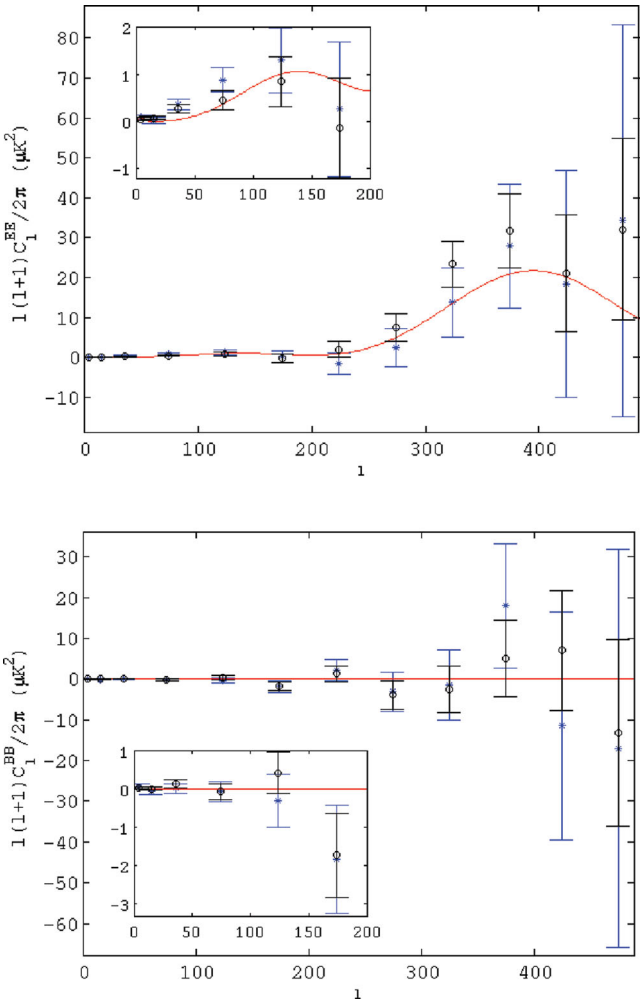

Figure 5. Polarization power spectrum EE (upper panel) and BB (lower panel) for the high-resolution analysis. The circles denote the spectrum supplied by the *WMAP* team and the asterisks represent our estimation. The solid line represents the fiducial model for C_ℓ^{EE} and the zero value for C_ℓ^{BB}.

at these scales is important. This was modelled better in Section 3, where a more accurate version of this information was available.

The resulting power spectra are presented in Fig. 5 . Our outcome is compatible with the analysis of the *WMAP* team, in which it is possible to distinguish the acoustic peak around $\ell \sim 400$ in the E-mode spectrum. As expected, the B-mode power spectrum is compatible with zero.

Our independent approach can be seen as a confirmation of the previous detection reported by the *WMAP* team.

A similar procedure is applied to determine the correlation between temperature and E-mode polarization data. We carry out the analysis using our cleaned maps of the Q and U Stokes parameters and the foreground reduced temperature maps that the *WMAP* team supplies. In this case, the combination of two maps of the same DA is allowed and equation (7) has the same form, as long as we add that, in C_ℓ^{AB}, A refers to the DA of the temperature maps and B to the DA of the polarization maps, with A, B $\in \{Q1, Q2, V2, W1, W2, W4\}$. For the temperature maps, we use the temperature-analysis mask that the *WMAP* team supplies, and the MASTER estimation is computed as is described in Kogut et al. (2003).

Because the CMB cosmic variance in temperature contributes significantly, we cannot ignore it this time in the calculation of the

[1] http://lambda.gsfc.nasa.gov/

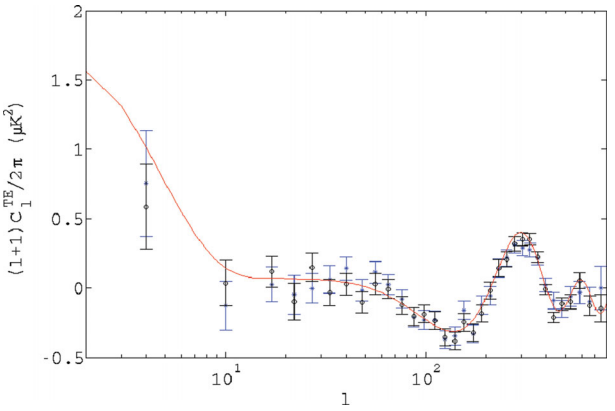

Figure 6. Polarization power spectrum TE. The circles denote the spectrum supplied by the *WMAP* team and the asterisks represent our estimation. The fiducial model is plotted by the solid line.

error bars. So, we generate 10^3 simulations of CMB plus noise, which undergo the same processes of cleaning and combination to obtain the cross-power spectrum, with which we estimate the error bars. These errors are relatively larger with respect to the *WMAP* results, because of the lower number of effective cross spectra. In addition, we remark that, while we use a pseudo-spectrum, a low-resolution analysis is performed through a pixel-base likelihood by the *WMAP* team.

The resulting cross-power spectrum is presented in Fig. 6 , and it is compatible with the power spectrum that the *WMAP* team supplies.

5 CONCLUSIONS

We introduce an internal template cleaning method that uses a wavelet decomposition on the sphere. Among its advantages, there is the possibility of multiresolution analysis, which allows an effective variation of the spectral index in the sky. A much lower computational time is needed than with other widely used continuous wavelets. In addition, a good treatment of incomplete sky coverage is given because of the compact support of the HW.

The result of the MITC method is a set of some cleaned maps at several frequencies that can be used, for instance, to verify whether any detected feature of the data is actually monochromatic or not. The exclusive use of internal templates allows us to analyse the maps without making any prior assumptions about the foregrounds in polarization. However, although the implementation that is shown here makes use of only internal templates, it can be trivially extended to deal with external templates as well.

We perform an analysis of the 7-yr *WMAP* data and we obtain outcomes that are compatible with the results of the *WMAP* team. Furthermore, we have evidence of better cleaning of the *Q*-band map at large scales, and we have obtained cleaned maps that are at least as good as those that the *WMAP* team supplies for the *V* and *W* bands. Let us remark that our approach does not make use of any additional template – everything is obtained from the *WMAP* data. We have checked that, although we use noisier templates, the instrumental-noise levels of the final cleaned maps are lower than those of the maps provided by the *WMAP* team.

High-resolution maps are also analysed. In agreement with the *WMAP* team, we find an E-mode detection at $\ell \sim 400$, as predicted by the standard ΛCDM model. We also find that the B-mode level is compatible with zero. These independent findings are a confirmation of the result already presented by the *WMAP* team.

The clean maps that we have produced, both at low and high resolution, are available at the following web site, http://max.ifca.unican.es/cobos/WMAP7yrPOL.

ACKNOWLEDGMENTS

We acknowledge partial financial support from the Spanish Ministerio de Ciencia e Innovación through projects AYA2010-21766-C03-01 and Consolider-Ingenio 2010 CSD2010-00064. RFC is gratefult for financial support from Spanish CSIC for a JAE-predoc fellowship. PV is grateful for financial support from the Ramón y Cajal program. We are grateful for the computer resources, technical expertise and assistance provided by the Spanish Supercomputing Network (RES) node at the University of Cantabria. We are grateful for the use of LAMBDA and the assistance provided by Benjamin Gold by e-mail. The HEALPIX package was used throughout the data analysis (Górski et al. 2005).

REFERENCES

Arnold K. et al., 2010, Proc. SPIE, 7741, 39
Baccigalupi C., Perrotta F., de Zotti G., Smoot G. F., Burigana C., Maino D., Bedini L., Salerno E., 2004, MNRAS, 354, 55
Baldi P., Kerkyacharian G., Marinucci D., Picard D., 2009, Annals of Statistics, 37, 1150
Betoule M., Pierpaoli E., Delabrouille J., Le Jeune M., Cardoso J.-F., 2009, A&A, 503, 691
Bonaldi A., Ricciardi S., Leach S., Stivoli F., Baccigalupi C., de Zotti G., 2007, MNRAS, 382, 1791
Brown M. L. et al., 2009, ApJ, 705, 978
Casaponsa B., Barreiro R. B., Curto A., Martínez-González E., Vielva P., 2011, MNRAS, 411, 2019
Charlassier R. et al., 2008, preprint (arXiv:0805.4527v1)
Delabrouille J., Cardoso J. F., 2007, preprint (astro-ph/0702198v2)
Delabrouille J., Cardoso J.-F., Le Jeune M., Betoule M., Fay G., Guilloux F., 2009, A&A, 493, 835
Efstathiou G., Gratton S., Paci F., 2009, MNRAS, 397, 1355
Eriksen H. K. et al., 2006, ApJ, 641, 665
Eriksen H. K., Jewell J. B., Dickinson C., Banday A. J., Górski K. M., Lawrence C. R., 2008, ApJ, 676, 10
Finkbeiner D. P., Davis M., Schlegel D. J., 1999, ApJ, 524, 867
Ghosh T., Delabrouille J., Remazeilles M., Cardoso J.-F., Souradeep T., 2011, MNRAS, 412, 883
Gold B. et al., 2011, ApJS, 192, 15
González-Nuevo J., Argüeso F., López-Caniego M., Toffolatti L., Sanz J. L., Vielva P., Herranz D., 2006, MNRAS, 369, 1603
Górski K. M., Hivon E., Banday A. J., Wandelt B. D., Hansen F. K., Reinecke M., Bartelmann M., 2005, ApJ, 622, 759
Grainger W. et al., 2008, Proc. SPIE, 7020, 68
Hansen F. K., Banday A. J., Eriksen H. K., Górski K. M., Lilje P. B., 2006, ApJ, 648, 784
Herranz D., Vielva P., 2010, IEEE Signal Processing Magazine, 27, 67
Hivon E., Górski K. M., Netterfield C. B., Crill B. P., Prunet S., Hansen F., 2002, ApJ, 567, 2
Jarosik N. et al., 2011, ApJS, 192, 14
Kim J., Naselsky P., Christensen P. R., 2009, Phys. Rev. D, 79, 023003
King O. G. et al., 2011, in AAS Meeting 217, 334.07
Kogut A. et al., 2003, ApJS, 148, 161
Kogut A. et al., 2006, New Astron. Rev., 50, 1009
Leach S. M. et al., 2008, A&A, 491, 597
Maino D., Donzelli S., Banday A. J., Stivoli F., Baccigalupi C., 2007, MNRAS, 374, 1207
Martínez-González E., Gallegos J. E., Argüeso F., Cayón L., Sanz J. L., 2002, MNRAS, 336, 22
Martínez-González E., Diego J. M., Vielva P., Silk J., 2003, MNRAS, 345, 1101

Rubiño-Martín J. A. et al., 2010, Highlights of Spanish Astrophysics V., p. 127
Sievers J. L. et al., 2009, preprint (arXiv:0901.4540v2)
Stivoli F., Grain J., Leach S. M., Tristram M., Baccigalupi C., Stompor R., 2010, MNRAS, 408, 2319
Tauber J. A. et al., 2010, A&A, 520, A1
Tucci M., Martínez-González E., Vielva P., Delabrouille J., 2005, MNRAS, 360, 935
Vielva P., Martínez-González E., Gallegos J. E., Toffolatti L., Sanz J. L., 2003, MNRAS, 344, 89